

Homotopy Simulation of Dissipative Micropolar Flow and Heat Transfer from a Two-Dimensional Body with Heat Sink Effect: Applications in Polymer Coating*



This work is licensed under a Creative Commons Attribution 4.0 International License

O. A. Bég,^a B. Vasu,^{b,*} A. K. Ray,^c T. A. Bég,^d A. Kadir,^a
H. J. Leonard,^a and R. S. R. Gorla^c

^aMulti-Physical Engineering Sciences Group, Aeronautical/Mechanical Engineering, SEE, Salford University, M54WT, UK

^bDepartment of Mathematics, Motilal Nehru National Institute of Technology, Allahabad, Prayagraj-211004, India

^cCentre of Applied Mathematics and Computing, ITER, Siksha 'O' Anusandhan, Bhubaneswar-751030, Odisha, India

^dEngineering Mechanics Research, Israfil House, Dickenson Rd., Manchester, M13, UK

^eDepartment of Aeronautics and Astronautics, Air Force Institute of Technology, Wright Patterson Air Force Base, Dayton, Ohio 45433, USA

<https://doi.org/10.15255/CABEQ.2020.1849>

Original scientific paper

Received: July 28, 2020

Accepted: December 13, 2020

Non-Newtonian flow from a wedge constitutes a fundamental problem in chemical engineering systems and is relevant to processing of polymers, coating systems, etc. Motivated by such applications, the homotopy analysis method (HAM) was employed to obtain semi-analytical solutions for thermal convection boundary layer flow of incompressible micropolar fluid from a two-dimensional body (wedge). Viscous dissipation and heat sink effects were included. The non-dimensional boundary value problem emerges as a system of nonlinear coupled ordinary differential equations, by virtue of suitable coordinate transformations. The so-called Falkner-Skan flow cases are elaborated. Validation of the HAM solutions was achieved with earlier simpler models, as well as with a Nakamura finite difference method for the general model. The micropolar model employed simulates certain polymeric solutions quite accurately, and features rotary motions of micro-elements. Primary and secondary shear stress, wall couple stress, Nusselt number, microrotation velocity, and temperature were computed for the effect of vortex viscosity parameter (micropolar rheological), Eckert number (viscous dissipation), Falkner-Skan (pressure gradient) parameter, micro-inertia density, and heat sink parameter. The special cases of Blasius and stagnation flow were also addressed. It was observed from the study that the temperature and thermal boundary layer thickness are both suppressed with increasing wedge parameter and wall heat sink effect, which is beneficial to temperature regulation in polymer coating dynamics. Further, strong reverse spin was generated in the microrotation with increasing vortex viscosity, which resulted in increase in angular momentum boundary layer thickness. Also, both primary and secondary skin friction components were reduced with increasing wedge parameter. Nusselt number was also enhanced substantially with greater wedge parameter.

Keywords:

micropolar fluid, wedge flow, homotopy analysis method, Nakamura difference scheme, pressure gradient, polymer flow processing

*Dedicated respectfully to the late Professor A. Cemal Eringen (1921–2009), [on the forthcoming centenary of his birth (2021)] formerly Emeritus Professor of Continuum Physics, Aerospace and Mechanical Engineering, Princeton University, New Jersey, USA, founder of the Society for Engineering Science (1963), for monumental contributions to microcontinuum fluid dynamics, multi-physical mechanics and rheological sciences, and for his mentorship to the first author from 2000–2008.

*Corresponding author: E-mail address: bvasu@mnnit.ac.in

Introduction

The flow from a two-dimensional wedge is a classical problem in viscous fluid mechanics and boundary layer theory, often referred to as Falkner-Skan flow¹. It has been extensively studied in industrial fluid dynamics, aerodynamics, applied mathematics, and chemical engineering transport phenomena, since it provides a good framework for

examining a variety of interesting flow cases, including flat plate (Blasius) flows, stagnation point flows, etc. It also features in certain polymer processing operations. The complex rheological characteristics (non-linear) of polymeric liquids generally lead to mathematical formulations which feature strongly coupled, multiple order differential equation systems. Considerable interest in computational and theoretical modelling of non-Newtonian wedge flows with and without heat transfer has emerged over the past two decades, following an early study by Peddieson², who used a Reiner-Rivlin differential viscoelastic model. Yacob *et al.*³ simulated steady nanofluid flow from a static or a moving wedge using Keller's box method and DO2HAF shooting routines. Hsu *et al.*⁴ employed a series expansion method to derive asymptotic solutions in terms of gamma functions, for viscoelastic Oldroyd fluid flow from a wedge of 90 degrees. Billingham and King⁵ employed asymptotic methods to study surface-tension driven flow from a slender wedge-shaped void. Su *et al.*⁶ used the differential transformation and base functions method (DTM-BF) to examine radiative flux and Joule dissipation effects on mixed magneto-convection from a stretching permeable wedge. Abbasbandy *et al.*⁷ studied the Falkner-Skan flow of magnetohydrodynamic (MHD) Maxwell fluids from a wedge, demonstrating that viscoelasticity exerts a strong influence on boundary layer thickness. Slip effects in Newtonian heat transfer flow from a wedge were investigated by Martin and Boyd⁸, for a range of Knudsen numbers. Bég *et al.*⁹ employed Nakamura's difference scheme to study non-similar viscoelastic convection from a wedge embedded in porous media (extending the Peddieson model²), elaborating in detail the influence of wedge geometry and buoyancy on thermal boundary layer characteristics. Hossain *et al.*¹⁰ used a local similarity numerical method to analyze the non-isothermal transient mixed convection from a sharp wedge, also presenting perturbation solutions for small and large dimensionless times. Kim¹¹ used the Ostwald-DeWaele power law model and shooting quadrature to investigate rheological flow in a porous medium, observing that for constant wedge angle and power-law rheological index, surface shear stress is lower for dilatant fluids compared with pseudo-plastic or Newtonian fluids. Rashidi *et al.*¹² used numerical shooting and homotopy methods to elaborate the effects of pressure-gradient parameter and viscoelasticity on heat transfer characteristics in third grade differential fluid flow from a non-isothermal wedge. Gorla¹³ considered the unsteady power-law non-Newtonian laminar thermal boundary layer flow over a wedge, addressing step changes in surface temperature and a large range of Prandtl numbers. Zueco *et al.*¹⁴ employed the elec-

tro-thermal network code, PSPICE, to investigate magnetic field and porous drag force effects on Nusselt number and skin friction in electrically-conducting gas convection over a wedge in permeable materials.

The aforementioned studies generally ignored the influence of heat sink (absorption) or viscous heating effects. In the manufacture of modern polymers, which are generally thermal insulators, heat sinks are frequently deployed on the body surface adjacent to the polymer to remove excess heat generated in viscous dissipation¹⁵. Heat sink performance is a function of material thermal conductivity. Utilizing heat sinks can counteract viscous heating effects and this can lead to thermally more stable plastics, and influences the efficiency of these materials in drawing heat away from potential application systems, e.g., electronic devices in servers, automobiles, high-brightness LEDs, aircraft wings, etc. In this regard, novel thermal interface materials are being introduced to mitigate reliability problems in the field, which may be caused by differential expansion in other thermally conductive polymeric materials¹⁶. A number of researchers have explored the influence of introducing heat sinks (or sources) on thermal convection boundary layer flows. Cheng and Huang¹⁷ reported numerical finite difference solutions for transient two-dimensional thermal convection from an accelerating surface with suction or blowing with heat generation (source) or absorption (sink) effects, considering both power-law surface temperature (PLST) and power-law heat flux (PLHF) boundaries. Kumar¹⁸ analyzed thermal radiation and heat sink effects on hydromagnetic stretching flow, using a confluent hypergeometric function (Kummer's function) for prescribed power-law wall temperature. Hassan *et al.*¹⁹ used finite volume computational software to model viscous dissipation effects on the temperature distribution throughout a rectangular channel for different polymers in mould injection, observing that in the case of low injection temperature, the viscous dissipation more strongly influences polystyrene than polypropylene, and causes a more pronounced non-uniform distribution of temperature through the polymer prior to the fluid achieving a thermally fully developed state. Further studies include Aydin²⁰ for forced convection pipe flow, Ahmad and Khan²¹ for internal heat generation/absorption in dissipative heat transfer from a porous moving wedge, Munir *et al.*²² for heat transfer in Sisko rheological dissipative flow from a wedge with variable free stream velocity, Bég *et al.*²³ for transient Hartmann-Couette magnetized convection. All these studies confirmed the strong influence of heat sinks and viscous dissipation (usually via the Eckert number) on thermo-fluid characteristics.

Although in many of the aforementioned articles, relatively comprehensive constitutive models have been implemented for non-Newtonian fluids^{24–27}, these models provide no insight into microstructural features. In many polymers, the suspensions significantly alter the viscosity characteristics. Eringen²⁸ introduced a robust mathematical framework for simulating such effects, namely, microcontinuum fluid mechanics. A simple example of the microfluid models is the micropolar model, which has also been modified by Eringen to include thermal effects²⁹. This model introduces angular momentum effects which have been shown to simulate³⁰ quite accurately numerous industrial, medical, and environmental flows, including liquid crystals, hemodynamics, air-borne pollutants, polymer melts, foodstuffs, and sediment transport in river beds. The theory of micropolar fluids simplifies the general micromorphic theory by restricting the form of the gyration tensor and physically represents suspensions comprising small, rigid cylindrical elements, such as large dumbbell-shaped molecules. These substructure particles can sustain rotary motions (microrotation) and support surface and body couples. Micropolar fluid dynamics has been an active area of research for almost five decades and continues to explore new applications. Bég *et al.*³¹ examined steady heat and mass transfer of micropolar boundary layer flow from a spherical body with Soret/Dufour effects. The Keller box numerical results showed that the micropolar vortex viscosity parameter reduces the flow near sphere. Gupta *et al.*³² employed a variational finite element method to evaluate the evolution of Sherwood number, Nusselt number, and wall couple stress functions with time, and buoyancy in unsteady convective heat and mass transfer in micropolar flow from a permeable extending wall. Prasad *et al.*³³ employed a Keller box numerical method to analyze the steady axisymmetric double-diffusive flow of a

micropolar nanofluid from a cylinder, calculating the influence of Brownian motion, thermophoresis, micro-inertial density, and Grashof number on angular velocity distributions. Recently, in the studies of micropolar transport phenomena, Pažanin and Suarez-Grau³⁴ addressed thin micropolar films, and Bég *et al.*³⁵ considered magnetohydrodynamic gravity-driven thin film micropolar flows.

In the present study, HAM, presently a very popular method in computational engineering sciences³⁶, was employed to develop solutions for the nonlinear, dissipative thermal convection boundary layer flow from a wedge with heat absorption effects. The influence of Eckert number, micropolar material viscosity, wedge angle, Prandtl number and heat sink parameter on angular velocity, temperature, linear velocity, and other characteristics was computed. Validation of HAM solutions with a tri-diagonal finite difference method due to Nakamura³⁷ is also presented. The current work is relevant to thermal polymeric processing and coating dynamics in chemical engineering technologies.

Mathematical model

Consider steady, two-dimensional, viscous, incompressible, forced convective heat transfer of a micropolar fluid from a wedge. It is assumed that the external velocity is in the form of $U = cx^m$, where c is a positive constant, $m = \beta^*/(2 - \beta^*)$ is the Hartree pressure gradient parameter which corresponds to $\beta^* = \Omega/\pi$ for an angle Ω of the wedge. The schematic diagram of the problem is shown in Fig. 1. The wedge lies in the x - y plane, with the x -coordinate orientated along the wedge front edge surface. The z -axis is orthogonal to the x - y plane.

Micropolar fluids are a special sub-class of simple microfluids²⁸. These fluids exhibit behaviour and properties which are influenced by the local motions of the material particles contained in each

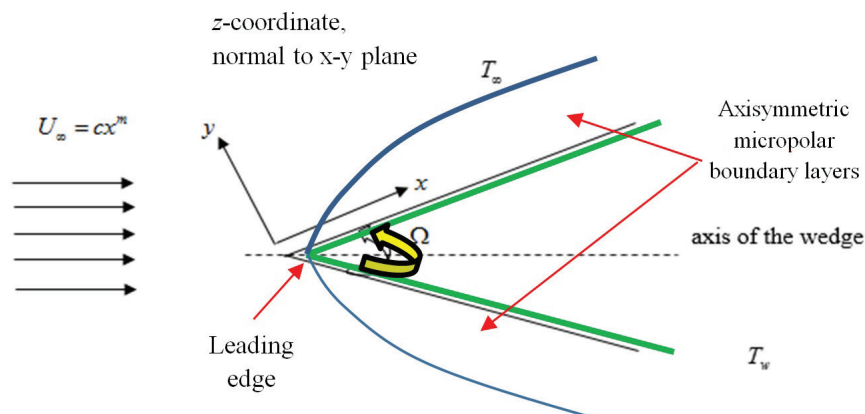


Fig. 1 – Physical model and coordinate system

of the volume elements, i.e., microelements. They possess local inertia. Micropolar fluids have volume elements containing rigid particles (non-deformable) which can spin about the centre of the volume element, and are defined by a microrotation vector. This local rotation of the particles is supplementary to the conventional rigid body motion of the entire volume element which defines Navier-Stokes fluids. In micropolar fluid mechanics, the classical continuum laws are therefore augmented with additional equations that account for the conservation of micro-inertia moments, and the balance of first stress moments which arise due to the consideration of microstructure in a fluid. Hence, new kinematic variables (gyration tensor, micro-inertia moment tensor), and concepts of body moments, stress moments and microstress are amalgamated with classical continuum fluid dynamics theory. The field equations for micropolar fluids in generalized form can be stated as^{28,30}:

conservation of mass

$$\frac{\partial \rho}{\partial t} + \nabla \cdot (\rho \mathbf{V}) = 0 \quad (1)$$

conservation of translational momentum

$$(\lambda + 2\mu + \kappa) \nabla \times \nabla \cdot \mathbf{V} - (\mu + \kappa) \nabla \times \nabla \times \mathbf{V} + \kappa \nabla \times \mathbf{G} - \nabla P + \rho \mathbf{f} = \rho \dot{\mathbf{V}} \quad (2)$$

conservation of angular momentum (microrotation)

$$(\alpha + \beta + \gamma) \nabla \times \nabla \cdot \mathbf{G} - \gamma \nabla \times \nabla \times \mathbf{G} + \kappa \nabla \times \mathbf{V} - 2\kappa \mathbf{G} + \rho \mathbf{l} = \rho j \dot{\mathbf{G}} \quad (3)$$

where ρ denotes the mass density of micropolar fluid, \mathbf{V} is translational velocity vector, \mathbf{G} is angular velocity (microrotation or gyration) vector, j is micro-inertia density, \mathbf{f} is the body force per unit mass vector, \mathbf{l} is the body couple per unit mass vector, P is the thermodynamic pressure, μ is the Newtonian dynamic viscosity, λ is the Eringen second order viscosity coefficient, κ is the vortex viscosity coefficient, and α , β and γ are spin gradient viscosity coefficients for micropolar fluids. In the micropolar model theory, we are only concerned with two independent kinematical vector fields; namely, the velocity vector field (familiar from Navier-Stokes theory), and the axial vector field which simulates the spin or the microrotations of the micropolar fluid particles, these being assumed non-deformable, i.e., rigid. We note that in micropolar fluid theory, for the case where the fluid has constant physical properties, no external body forces exist, and for steady-state flow, the conservation equations can be greatly simplified. Additionally, for the case where $\kappa = \alpha = \beta = \gamma = 0$ and with vanishing \mathbf{l} and \mathbf{f} , the gyration vector disappears and equation (3) vanishes. Equa-

tion (2) also reduces in this special case to the classical Navier-Stokes equations (Newtonian viscous flow model). We also note that, for the case of zero vortex viscosity only, the velocity vector \mathbf{V} and the microrotation \mathbf{G} are decoupled and the global motion is unaffected by the microrotations. This model was applied to the axisymmetric wedge scenario with a constant heat flux applied at the wedge surface. T_∞ of the ambient fluid (free stream) is assumed to be constant. Assuming constant spin gradient viscosity of the micropolar fluid, neglecting momentum and thermal variations in the z -direction^{1,5} and assuming that the micro-elements are non-deformable, the equations for mass continuity, momentum, and energy can be written as follows:

mass conservation

$$\frac{\partial u}{\partial x} + \frac{\partial v}{\partial y} = 0, \quad (4)$$

x -direction linear (translational) momentum conservation:

$$\rho \left(u \frac{\partial u}{\partial x} + v \frac{\partial u}{\partial y} \right) = (\mu + \kappa) \left(\frac{\partial^2 u}{\partial y^2} \right) + \kappa \frac{\partial N}{\partial y} + \rho U \frac{dU}{dx} \quad (5)$$

z -direction linear (translational) momentum conservation:

$$\rho \left(u \frac{\partial w}{\partial x} + v \frac{\partial w}{\partial y} \right) = (\mu + \kappa) \left(\frac{\partial^2 w}{\partial y^2} \right) \quad (6)$$

angular momentum (microrotation) conservation:

$$\rho \left(u \frac{\partial N}{\partial x} + v \frac{\partial N}{\partial y} \right) = \frac{\gamma}{j} \left(\frac{\partial^2 N}{\partial y^2} \right) - \frac{\kappa}{j} \left(\frac{\partial u}{\partial y} + 2N \right), \quad (7)$$

energy (heat) conservation:

$$\rho c_p \left(u \frac{\partial T}{\partial x} + v \frac{\partial T}{\partial y} \right) = k \left(\frac{\partial^2 T}{\partial y^2} \right) + (\mu + \kappa) \left(\left(\frac{\partial u}{\partial y} \right)^2 + \left(\frac{\partial w}{\partial y} \right)^2 \right) + Q(T - T_\infty) \quad (8)$$

where u denotes translational velocity along the x -direction, v is the translational velocity along the y -direction, N is the angular velocity (microrotation) component in the x - y plane, $\gamma = (\mu + \kappa/2)j$ is the Eringen spin gradient viscosity, T is fluid temperature, c_p denotes specific heat at constant pressure (isobaric), k is thermal conductivity of the micropolar fluid, and Q is the heat sink parameter (negative). The appropriate boundary conditions^{31,66} are prescribed at the wedge surface and the edge of the boundary layer regime on the wall (far from the wedge), and take the form:

$$\text{At } y = 0 : u = 0, \quad v = 0, \quad w = 0, \quad N = -n \frac{\partial u}{\partial y}, \quad q_w = -k \frac{\partial T}{\partial y} \tag{9a}$$

$$\text{At } y \rightarrow \infty : u \rightarrow U = cx^m; w \rightarrow 0, N \rightarrow 0, T \rightarrow T_\infty \tag{9b}$$

In Eq. (9b), the parameter m has several important values corresponding to classical flow configurations. Four cases are noteworthy:

Case I: Generalized two-dimensional wedge flow for which $0 < \beta^* < 2$ i.e. $m > 0$.

Case II: Flow past a semi-infinite horizontal surface (flat plate) when $\beta^* \rightarrow 0$ for which $m = 0$.

Case III: Forward stagnation point flow adjacent to a vertical surface (this case also amounts to linear free stream velocity variation with axial distance) when $\beta^* \rightarrow 1$ for which $m = 1$.

Case IV: Rear stagnation-point flow when $\beta^* \rightarrow -1$ for which $m = -1/3$.

The first three cases are most relevant to polymeric coating processes. These cases are also entirely valid when heat transfer is considered. Details of the microrotation boundary conditions, controlled by the parameter n in (9), allow a variety of physical scenarios to be considered. Here we elect the case with $n = 0.5$ which corresponds to weak con-

centration of micro-elements at the wall. The cases $n = 0$ and $n = 1$ are associated, respectively, with strong near-wall concentrations and turbulent flows, neither of which are relevant in the present analysis. The micropolar fluid model therefore introduces both a separate angular momentum balance as well as supplementary boundary conditions. Inspection of equations (5) and (7) also reveals that there is a strong coupling between the angular velocity and primary translational velocity fields, although there are no mixed derivatives, as encountered in certain viscoelastic models. The parabolic partial differential equations (4)–(8) are still very challenging to solve. It is possible therefore to transform the boundary value problem to yield more amenable numerical solutions. We therefore define the following scaling transformations and non-dimensional variables, and introduce a stream function ψ , defined by $u = \frac{\partial \psi}{\partial y}$ and $v = -\frac{\partial \psi}{\partial x}$, which automatically satisfies the mass conservation:

$$\eta = \left(\frac{(m+1)U}{2\nu x} y \right)^{1/2}, \quad \psi = \left(\frac{2\nu x U}{(m+1)} \right)^{1/2} F(\eta), \quad w = UG(\eta), \quad N = UH(\eta) \left(\frac{(m+1)U}{2\nu x} \right)^{1/2},$$

$$\theta(\eta) = \frac{k(T - T_\infty)}{q_w} \left(\frac{(m+1)U}{2\nu x} \right)^{1/2}, \quad \Phi = \left(\frac{2xQ(x)}{\rho c_p U} \right), \quad K = \frac{\kappa}{\mu}, \quad I = \frac{\nu^2 Re}{j c_p (T - T_\infty)} \tag{10}$$

where η is the pseudo-similarity coordinate in the y -direction, F is dimensionless stream function, G is dimensionless secondary velocity, H is dimensionless angular velocity (microrotation), θ is dimensionless temperature function, Φ is heat sink parameter (negative), K is the vortex viscosity parameter, I is the dimensionless micro-inertia density param-

eter, Ec is the Eckert (viscous dissipation) number, and Re is Reynolds number. Equations (4) – (8) are thereby reduced to the following ninth order system of coupled, non-linear ordinary differential equations, describing the dimensionless linear and angular velocity fields and temperature field:

primary momentum

$$(1 + K) \frac{d^3 F}{d\eta^3} + F \frac{d^2 F}{d\eta^2} - \frac{2m}{m+1} \left(1 - \left(\frac{dF}{d\eta} \right)^2 \right) + K \frac{dH}{d\eta} = 0 \tag{11}$$

secondary momentum

$$(1 + K) \frac{d^2 G}{d\eta^2} + F \frac{dG}{d\eta} - \frac{2m}{m+1} G \frac{dF}{d\eta} = 0 \tag{12}$$

angular momentum

$$(1 + K) \frac{d^2 H}{d\eta^2} - \left(\left(\frac{3m-1}{m+1} \right) H \frac{dF}{d\eta} - F \frac{dH}{d\eta} \right) - \frac{2KI}{m+1} \left(2H + \frac{d^2 F}{d\eta^2} \right) = 0 \tag{13}$$

energy

$$\frac{1}{Pr} \frac{d^2 \theta}{d\eta^2} + \left((m-1) \frac{dF}{d\eta} + (1+K) Ec \left\{ \left\langle \frac{d^2 F}{d\eta^2} \right\rangle^2 + \left\langle \frac{dG}{d\eta} \right\rangle^2 \right\} + \Phi \right) \theta + (m-1) F \frac{d\theta}{d\eta} \tag{14}$$

The corresponding transformed boundary conditions are specified as:

$$\text{At } \eta = 0: F(0) = 0; \frac{dF(0)}{d\eta} = 0; G(0) = 0; H(0) = -0.5 \frac{d^2F(0)}{d\eta^2}; \frac{d\theta(0)}{d\eta} = -1 \quad (15)$$

$$\text{As } \eta \rightarrow \infty: \frac{dF}{d\eta}(\infty) \rightarrow 1; G(\infty) = H(\infty) = \theta(\infty) \rightarrow 0 \quad (16)$$

In engineering simulations, we are interested not only in the velocity, microrotation, and temperature functions, but also certain gradient functions of these variables. The non-dimensional primary and secondary wall shear stress, i.e., skin friction, are defined thus:

$$C_{f_x,p} = \frac{2\tau_x}{\rho U^2} = \frac{2}{\rho U^2} \left((\mu + \kappa) \frac{\partial u}{\partial y} + \kappa N \right)_{y=0} = \left(\frac{2(m+1)}{\text{Re}} \right)^{1/2} \left(1 + \frac{K}{2} \right) \frac{d^2F(0)}{d\eta^2} \quad (17)$$

$$C_{f_x,s} = \frac{2\tau_w}{\rho U^2} = \frac{2}{\rho U^2} \left((\mu + \kappa) \frac{\partial w}{\partial y} \right)_{y=0} = \left(\frac{2(m+1)}{\text{Re}} \right)^{1/2} (1+K) \frac{dG(0)}{d\eta} \quad (18)$$

Dimensionless wall couple stress is computed from:

$$M_w = \frac{m_w}{\rho U^2 L} = \frac{\gamma \frac{\partial N}{\partial y} \Big|_{y=0}}{\rho U^2 L} = \left(\frac{2(m+1)}{\text{Re}} \right)^{1/2} \frac{dH(0)}{d\eta} \quad (19)$$

The dimensionless local Nusselt number (wedge surface heat transfer rate) is given by:

$$\text{Nu} = \frac{xq_w}{k(T - T_\infty)} = \frac{-x \frac{\partial T}{\partial y} \Big|_{y=0}}{(T - T_\infty)} = - \left(\frac{(m+1)\text{Re}}{2} \right)^{1/2} \frac{d\theta(0)}{d\eta} \quad (20)$$

where τ_x is the primary dimensional wall shear stress, τ_w is the secondary dimensional wall shear stress, m_w is the dimensional wall couple stress, U is the characteristic velocity, and L is an arbitrary scale length. We note that skin friction, wall couple stress, and wall heat transfer rate can be in fact studied by simply computing

the gradients $\frac{d^2F(0)}{d\eta^2}$, $\frac{dG(0)}{d\eta}$, $\frac{dH(0)}{d\eta}$ and $\frac{d\theta(0)}{d\eta}$. The set of ordinary differential equations (11)–(14) are

highly nonlinear and analytical solutions are intractable. We therefore developed semi-numerical solutions using the homotopy analysis method (HAM). The methodology is described further herein. Several important special cases of the present flow model may be retrieved. The flow model describes Newtonian convection as $K \rightarrow 0$. When $Ec = 0$ viscous heating is negated and when $\Phi = 0$ heat sink vanishes. For $m = 0$ the wedge flow becomes Blasius flow from a flat plate. With $m = 1$, we retrieve the case of flow in the vicinity of a stagnation point on an infinite plate.

Homotopy Analysis Method (HAM) solution

The transformed non-dimensional boundary value problem defined by Eqs. (11)–(14) with boundary conditions (15), (16) is of ninth order, multi-degree, strongly non-linear and coupled. Many different techniques are available for the solution of this system. Here, the homotopy analysis method (HAM) was selected, which is an exceptionally accurate and robust semi-analytic method developed originally by Liao³⁶ and has been used by many mathematicians and researchers in numerous different fields of engineering science, including vibration, fluid dynamics, medicine, and energy systems. Recent applications include coating nanofluid dynamics on a sphere³⁸, viscoplastic magnetic bio-

convection stretching sheet flow³⁹, biological propulsion⁴⁰, structural dynamics of functional plates⁴¹, thin film rheological nanofluid flow⁴² and external nanofluid convection boundary layers⁴³. A modern perspective HAM has also been given by Liao⁴⁴. Liao and Chwang⁴⁵ have applied HAM to simulate non-linear oscillations in structural dynamics. Jangili and Bég⁴⁶ deployed HAM to compute the entropy generation in electromagnetic micropolar convection flow in a vertical duct. Arafa *et al.*⁴⁷ used HAM to analyse the transient behaviour of a biochemical reaction model. Recently, Ray *et al.*⁴⁸ used HAM in order to obtain non-similar solution to the mixed convective flow of non-Newtonian Eyring-Powell fluid due to convectively heated vertical plate. Shukla *et al.*⁴⁹ simulated the hydromag-

netic slip free and forced convection coating flow of a nanoliquid on an upright cylindrical body, also conducting a second law thermodynamic analysis. Ray *et al.*⁵⁰ and Vasu and Ray⁵¹ have also implemented HAM to study the flow of non-Newtonian

fluid over a plate with oscillating motion. All these studies have confirmed the impressive versatility of HAM. For the current problem, implementing HAM, the following initial approximations of F , G , H and θ are defined:

$$F_0 = \eta - 1 + e^{-\eta}, \quad G_0 = e^{-\eta} - e^{-\eta/2}, \quad H_0 = -0.5e^{-\eta} \text{ and } \theta_0 = e^{-\eta} \tag{21}$$

The following *linear operators* are chosen:

$$L_1(F) = F''' - F', \quad L_2(G) = G'' - G, \quad L_3(H) = H'' - H \text{ and } L_4(\theta) = \theta'' - \theta \tag{22}$$

These satisfy the properties:

$$L_1(c_1 + c_2e^\eta + c_3e^{-\eta}) = 0, \quad L_2(c_4e^\eta + c_5e^{-\eta}) = 0, \quad L_3(c_6e^\eta + c_7e^{-\eta}) = 0 \text{ and } L_4(c_8e^\eta + c_9e^{-\eta}) = 0 \tag{23}$$

Here c_i ($1 \leq i \leq 5$) are arbitrary constants. If $0 \leq p \leq 1$ is the embedding parameter and $\hbar_1, \hbar_2, \hbar_3$ and \hbar_4 are respective convergence control parameters, then we can construct the zeroth-order deformation equations as

$$(1 - p)L_1[F(\eta; p) - F_0(\eta)] = p\hbar_1 N_1[F(\eta; p), G(\eta; p), H(\eta; p), \theta(\eta; p)] \tag{24}$$

$$(1 - p)L_2[G(\eta; p) - G_0(\eta)] = p\hbar_2 N_2[F(\eta; p), G(\eta; p), H(\eta; p), \theta(\eta; p)] \tag{25}$$

$$(1 - p)L_3[H(\eta; p) - H_0(\eta)] = p\hbar_3 N_3[F(\eta; p), G(\eta; p), H(\eta; p), \theta(\eta; p)] \tag{26}$$

$$(1 - p)L_4[\theta(\eta; p) - \theta_0(\eta)] = p\hbar_4 N_4[F(\eta; p), G(\eta; p), H(\eta; p), \theta(\eta; p)] \tag{27}$$

The boundary conditions (15), (16) take the form:

$$F(0; p) = 0; \quad \frac{dF(0; p)}{d\eta} = 0; \quad G(0; p) = 0; \quad H(0; p) = -0.5 \frac{d^2F(0; p)}{d\eta^2}; \quad \frac{d\theta(0; p)}{d\eta} = -1 \tag{28}$$

$$\frac{dF(\infty; p)}{d\eta} \rightarrow 1; \quad G(\infty; p) = H(\infty; p) = \theta(\infty; p) \rightarrow 0$$

Depending upon Eqs. (11)–(16), the nonlinear homotopy operators are next defined:

$$N_1(F(\eta; p), G(\eta; p), H(\eta; p), \theta(\eta; p)) = (1 + K) \frac{d^3F(\eta; p)}{d\eta^3} + F(\xi, \eta; p) \frac{d^2F(\eta; p)}{d\eta^2} - \frac{2m}{m+1} \left(1 - \left(\frac{dF(\eta; p)}{d\eta} \right)^2 \right) + K \frac{dH(\eta; p)}{d\eta} \tag{29}$$

$$N_2(F(\eta; p), G(\eta; p), H(\eta; p), \theta(\eta; p)) = (1 + K) \frac{d^2G(\eta; p)}{d\eta^2} + F(\eta; p) \frac{dG(\eta; p)}{d\eta} - \frac{2m}{m+1} G(\eta; p) \frac{dF(\eta; p)}{d\eta} \tag{30}$$

$$N_3(F(\eta; p), G(\eta; p), H(\eta; p), \theta(\eta; p)) = (1 + K) \frac{d^2H(\eta; p)}{d\eta^2} - \left(\left(\frac{3m-1}{m+1} \right) H(\eta; p) \frac{dF(\eta; p)}{d\eta} - F(\eta; p) \frac{dH(\eta; p)}{d\eta} \right) - \frac{2KI}{m+1} \left(2H(\eta; p) + \frac{d^2F(\eta; p)}{d\eta^2} \right) \tag{31}$$

$$N_4(F(\eta; p), G(\eta; p), H(\eta; p), \theta(\eta; p)) = \frac{1}{Pr} \frac{d^2\theta(\eta; p)}{d\eta^2} + \left((m-1) \frac{dF(\eta; p)}{d\eta} + (1+K)Ec \left\{ \left\langle \frac{d^2F(\eta; p)}{d\eta^2} \right\rangle^2 + \left\langle \frac{dG(\eta; p)}{d\eta} \right\rangle^2 \right\} + \Phi \right) \theta(\eta; p) + (m-1)F(\eta; p) \frac{d\theta(\eta; p)}{d\eta} \tag{32}$$

For $p = 0$ and $p = 1$, we have:

$$\begin{aligned} F(\eta; 0) &= F_0(\eta) & F(\eta; 1) &= F(\eta) \\ G(\eta; 0) &= G_0(\eta) & G(\eta; 1) &= G(\eta) \\ H(\eta; 0) &= H_0(\eta) & H(\eta; 1) &= H(\eta) \\ \theta(\eta; 0) &= \theta_0(\eta) & \theta(\eta; 1) &= \theta(\eta) \end{aligned} \quad (33)$$

It is noted that, as p rises from 0 to 1, then $F(\eta; p)$, $G(\eta; p)$, $H(\eta; p)$ and $\theta(\eta; p)$ vary from the initial guesses, $F_0(\eta)$, $G_0(\eta)$, $H_0(\eta)$ and $\theta_0(\eta)$ to the exact solutions $F(\eta)$, $G(\eta)$, $H(\eta)$ and $\theta(\eta)$ respectively.

Now expanding $F(\eta; p)$, $G(\eta; p)$, $H(\eta; p)$ and $\theta(\eta; p)$ in Taylor series with respect to p , we have:

$$F(\eta; p) = F_0(\eta) + \sum_{m=1}^{\infty} F_m(\eta) p^m, \quad F_m(\eta) = \frac{1}{m!} \frac{\partial^m F(\eta; q)}{\partial p^m} \Big|_{p=0} \quad (34)$$

$$G(\eta; p) = G_0(\eta) + \sum_{m=1}^{\infty} G_m(\eta) p^m, \quad G_m(\eta) = \frac{1}{m!} \frac{\partial^m G(\eta; q)}{\partial p^m} \Big|_{p=0} \quad (35)$$

$$H(\eta; p) = H_0(\eta) + \sum_{m=1}^{\infty} H_m(\eta) p^m, \quad H_m(\eta) = \frac{1}{m!} \frac{\partial^m H(\eta; q)}{\partial p^m} \Big|_{p=0} \quad (36)$$

$$\theta(\eta; p) = \theta_0(\eta) + \sum_{m=1}^{\infty} \theta_m(\eta) p^m, \quad \theta_m(\eta) = \frac{1}{m!} \frac{\partial^m \theta(\eta; q)}{\partial p^m} \Big|_{p=0} \quad (37)$$

If the initial guess, auxiliary linear operators and convergence control parameter are judiciously selected such that the series defined in Eqs. (34)–(37) are convergent at $p=1$, then:

$$F(\eta) = F_0(\eta) + \sum_{m=1}^{\infty} F_m(\eta) \quad (38)$$

$$G(\eta) = G_0(\eta) + \sum_{m=1}^{\infty} G_m(\eta) \quad (39)$$

$$H(\eta) = H_0(\eta) + \sum_{m=1}^{\infty} H_m(\eta) \quad (40)$$

$$\theta(\eta) = \theta_0(\eta) + \sum_{m=1}^{\infty} \theta_m(\eta) \quad (41)$$

The corresponding general series solution can be written as:

$$\begin{aligned} F_m(\eta) &= F_m^*(\eta) + c_1 + c_2 e^\eta + c_3 e^{-\eta}, & G_m(\eta) &= G_m^*(\eta) + c_4 e^\eta + c_5 e^{-\eta} \\ H_m(\eta) &= H_m^*(\eta) + c_6 e^\eta + c_7 e^{-\eta} & \text{and } \theta_m(\eta) &= \theta_m^*(\eta) + c_8 e^\eta + c_9 e^{-\eta} \end{aligned} \quad (42)$$

Here $F_m^*(\eta)$, $G_m^*(\eta)$, $H_m^*(\eta)$ and $\theta_m^*(\eta)$ are special solutions. Within Mathematica symbolic software, HAM is employed in order to solve the Eqs. (11)–(16) with the correctly specified quantities which are critical to this method, i.e., initial guesses (21), auxiliary linear operators (22), and non-linear operators (29)–(32). After the proper selection of initial guess and operators, the range of non-zeroes auxiliary parameter is obtained, and this is visualized in Fig. 2(a) and Fig. 2(b). A crucial feature of HAM is convergence. HAM exhibits considerable sensitivity to the auxiliary parameter \hbar , Fig. 2 ((a) and (b)) show the \hbar -curves for the range of \hbar_1 , \hbar_2 ,

\hbar_3 and \hbar_4 for F , G , H and θ , respectively. After proper selection of the initial guess and operators, the range of non-zero auxiliary parameter is obtained. The ranges for the non-zero parameters \hbar_1 , \hbar_2 and \hbar_3 are $-1 < \hbar_1 < -0.23$, $-0.6 < \hbar_2 < -0.15$, $-0.7 < \hbar_3 < -0.1$ and all values of \hbar_4 (using Eq. (19)) with 10th order of approximation when $Pr=100$, $K=0.5$, $I=0.5$, $\Phi=-0.5$, $m=0.3$, $Ec=0.2$. Table 1 shows that negligible variation is observed for orders of approximation higher than the 10th order. Hence, we have taken the 10th order of approximation for all computations.

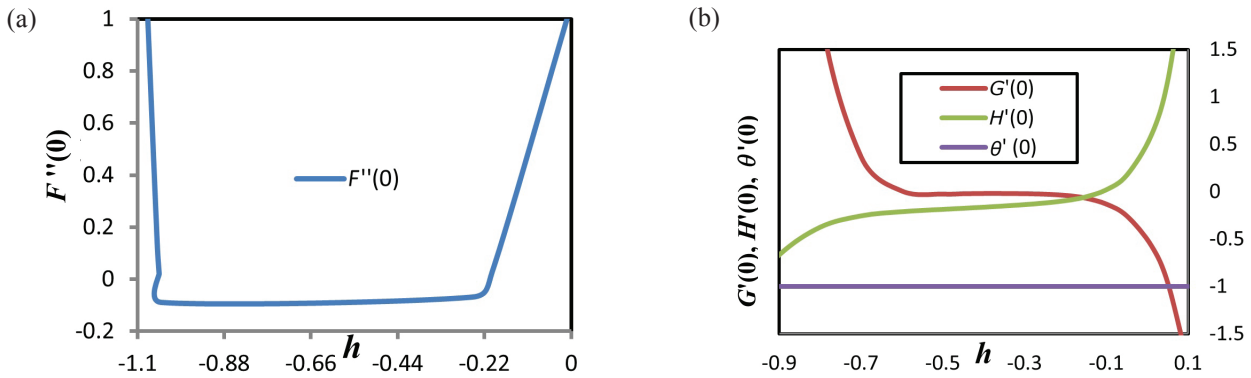


Fig. 2 – (a) h -curve; (b) h -curve

Table 1 – Convergence of HAM series solution

Order	$F''(0)$	$G'(0)$	$H'(0)$	$\theta(0)$
4	0.4154055	-0.180111	0.123112	-1
5	0.38686	-0.179081	0.119438	-1
6	0.36723787	-0.178815	0.117465	-1
8	0.34263235	-0.178030	0.115332	-1
9	0.3349536	-0.182061	0.114917	-1
10	0.32786463	-0.171249	0.11408	-1
11	0.32532043	-0.177313	0.115215	-1
12	0.32377995	-0.179062	0.110351	-1

Validation with Nakamura Tridiagonal Method (NTM)

The present study is novel and therefore no comparable studies exist in the literature for verifying the HAM computations. Therefore, to validate the present HAM solutions, an efficient finite difference procedure of the implicit type, originally developed by Nakamura³⁷, was utilized to solve the entire ninth order boundary value problem defined by Eqs. (11)–(14) under boundary conditions (15, 16). As with other finite difference schemes, a reduction of the higher order differential equations arising is intrinsic also to the Nakamura tridiagonal method (NTM). NTM is also particularly accurate at simulating parabolic problems as exemplified by boundary layer flows. Applications of NTM include elastic stability of nanostructures⁵², bioconvection⁵³, magnetohydrodynamic nanofluid flow⁵⁴. Further details are documented in the extensive review by Bég⁵⁵ and the article by Nakamura⁵⁶. NTM works well for both one-dimensional (ordinary differential equation systems) and two-dimensional (partial differential) non-similar flows. NTM entails a combination of the following aspects.

(i) The flow domain for the convection field is discretized using an equi-spaced finite difference mesh in the η -direction.

(ii) The ordinary derivatives for F, G, H, θ with respect to η are evaluated by central difference approximations.

(iii) A single iteration loop based on the method of successive substitution is utilized due to the high nonlinearity of the primary/secondary momentum, angular momentum, and energy conservation equations.

(iv) The finite difference discretized equations are solved as a linear second order boundary value problem of the ordinary differential equation type on the η -domain.

All the conservation equations, except the primary linear momentum Eq. (11), are second order equations, and for these Eqs., i.e., (12), (13), (14), only a direct substitution is needed. Setting:

$$P = F' \tag{43}$$

$$Q = G \tag{44}$$

$$R = H \tag{45}$$

$$S = \theta \tag{46}$$

Eqs. (11)–(14) then assume the form:

Nakamura primary momentum equation:

$$A_1 P'' + B_1 P' + C_1 P = S_1 \tag{47}$$

Nakamura secondary momentum equation:

$$A_2 Q'' + B_2 Q' + C_2 Q = S_2 \tag{48}$$

Nakamura angular momentum equation:

$$A_3 R'' + B_3 R' + C_3 R = S_3 \tag{49}$$

Nakamura energy equation:

$$A_4 S'' + B_4 S' + C_4 S = S_4 \tag{50}$$

where $A_{i=1...4}, B_{i=1...4}, C_{i=1...4}$ are the Nakamura matrix coefficients, $S_{i=1...4}$ are the Nakamura source terms containing a mixture of variables and derivatives associated with the variables. The Nakamura Eqs. (47)–(50) are transformed to finite difference equa-

Table 2 – Effect of parameters on primary skin friction, $(Re)^{1/2} C_{f_p}$

Parameters	HAM	NTM
$m = 0$	0.844946	0.844901
$m = 0.1$	0.591388	0.591372
$m = 0.3$	0.018006	0.017943
$k = 0$	0.02575	0.025684
$k = 0.2$	0.025556	0.025581
$k = 0.5$	0.018006	0.018034
$I = 0$	0.030319	0.030296
$I = 0.1$	0.027331	0.027352
$I = 0.5$	0.018006	0.018013

Table 3 – Effect of parameters on secondary skin friction, $(Re)^{1/2} C_{f_s}$

Parameters	HAM	NTM
$m = 0$	-0.07726	-0.07703
$m = 0.1$	-0.07303	-0.07295
$m = 0.3$	-0.08337	-0.08312
$k = 0$	-0.11008	-0.11014
$k = 0.2$	-0.09812	-0.09823
$k = 0.5$	-0.08337	-0.08317
$I = 0$	-0.08339	-0.08328
$I = 0.1$	-0.08338	-0.08319
$I = 0.5$	-0.08337	-0.08324

tions and these are orchestrated to form a tridiagonal system which is solved iteratively. Mesh independence testing was conducted and after some experimentation, 150 cells (steps) were selected since denser grids failed to modify the solution tangibly. The benchmarks with HAM solutions for $Pr = 100$ (polymer coating) are documented in Tables 2–5, for $\frac{d^2F(0)}{d\eta^2}$ (primary shear stress), $\frac{dG(0)}{d\eta}$ (secondary shear stress), $\frac{dH(0)}{d\eta}$ (wall couple stress), and $\frac{d\theta(0)}{d\eta}$ (Nusselt number function), respectively.

The default data for these tables is $\Phi = -0.5$ (heat sink), $Pr = 100$ (weak polymers) with $Ec = 0.2$ (dissipation present).

Inspection of Tables 2–5 confirms excellent agreement between the HAM and NTM codes. Confidence in the MATLAB HAM solutions is therefore justifiably high. Further interpretation of these Tables will be provided in due course.

Table 4 – Effect of parameters on dimensionless wall couple stress, $(Re)^{1/2} M_w$

Parameters	HAM	NTM
$m = 0$	0.018126	0.01813
$m = 0.1$	-0.0231	-0.02322
$m = 0.3$	-0.16241	-0.16249
$k = 0$	-0.112	-0.11207
$k = 0.2$	-0.14302	-0.14314
$k = 0.5$	-0.16241	-0.16253
$I = 0$	-0.09822	-0.09798
$I = 0.1$	-0.11437	-0.11421
$I = 0.5$	-0.16241	-0.16244

Table 5 – Effect of parameters on Nusselt number, $(Re)^{-1/2} Nu$

Parameters	HAM	NTM
$m = 0$	0.707107	0.707122
$m = 0.1$	0.74162	0.741633
$m = 0.3$	0.806226	0.806234
$k = 0$	0.806226	0.806234
$k = 0.2$	0.806226	0.806234
$k = 0.5$	0.806226	0.806234
$I = 0$	0.806226	0.806234
$I = 0.1$	0.806226	0.806234
$I = 0.5$	0.806226	0.806234

HAM results and discussion

Extensive computations were conducted. These are plotted in Figs. 3–13, and illustrate the impact of 5 thermophysical parameters (K , Ec , Φ , m , I) on the microrotation (angular velocity), H , temperature, θ , and primary velocity ($dF/d\eta$). Prandtl number is constrained at $Pr = 100$ which corresponds to low eight polymers (coatings), as noted in Incropera and Dewitt⁵⁷.

Fig. 3 shows that increasing values of the micro-inertia density parameter, I , induce a substantial decrease in angular velocity of micro-elements, i.e., increasingly negative values. This corresponds to a reversal in spin of micro-elements. The surface condition imposed at the wedge wall implies weak micro-element rotation ($n = 0.5$, for which the anti-symmetric component of the stress tensor vanishes, as noted by Eringen²⁹), since gyratory motions are still largely inhibited by the boundary. The parameter

$$I = \frac{v^2 Re}{jU^2 \frac{U^2}{c_p (T - T_\infty)}}$$

rotation conservation Eq. (13) in the term, $-\frac{2KI}{m+1}\left(2H + \frac{d^2F}{d\eta^2}\right)$. This acts as a negative body force, and the direct proportionality to I implies that

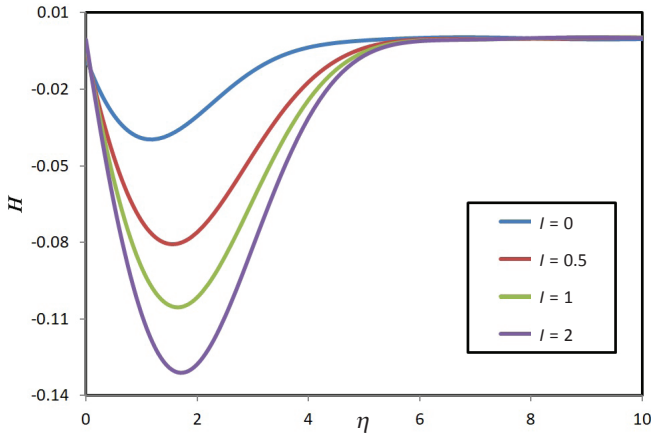


Fig. 3 – H (angular velocity) versus η for $K = 0.5$, $Ec = 0.2$, $\Phi = -0.5$ (heat sink), $Pr = 100$ (weak polymers), $m = 0.3$ (general wedge flow) with micro-inertia density parameter (I)

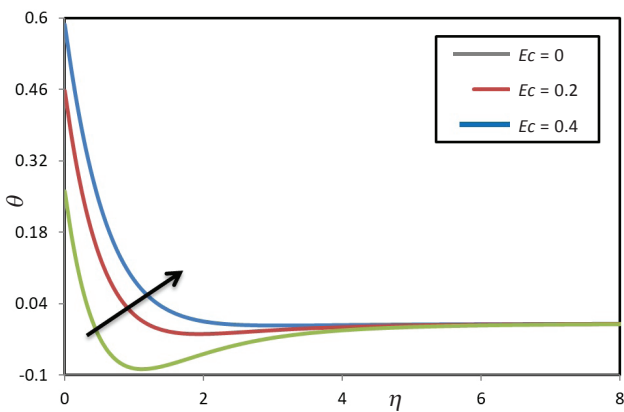


Fig. 4 – θ (temperature) versus η for $K = 0.5$, $I = 0.5$, $\Phi = -0.5$ (heat sink), $Pr = 100$ (weak polymers), $m = 0.3$ (general wedge flow) with Eckert number

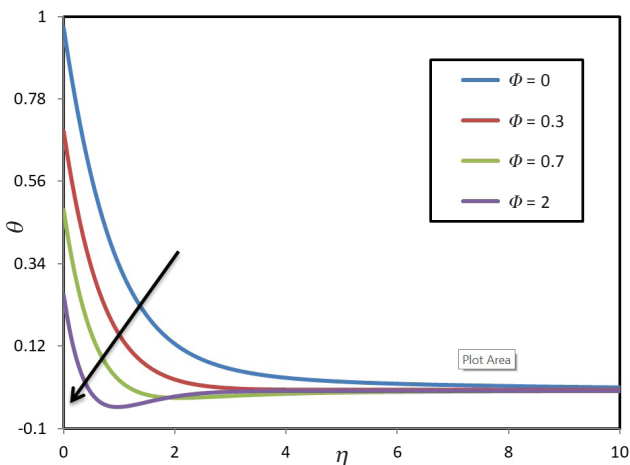


Fig. 5 – θ (temperature) versus η for $K = 0.5$, $I = 0.5$, $Ec = 0.2$, $Pr = 100$ (weak polymers), $m = 0.3$ (general wedge flow) with $\Phi = 0$ (no heat sink), -0.3 , -0.7 , -2.0

larger values of I impede the rotation of micro-elements. The effect is prominent enough to induce counter-rotation of micro-elements, i.e., reverse spin. Asymptotically smooth profiles were computed in the free stream for which microrotation vanishes, confirming the imposition of an adequately large infinity boundary condition. The trends concur with earlier studies by Hassanien and Salama⁵⁸, Mostafa *et al.*⁵⁹ and Nath⁶⁰. It is also noteworthy that the case $I = 0$ does not correspond to a Newtonian fluid as incorrectly implied in several studies), but to the case where micro-inertia density has no contribution to the microrotation field, and supplementary terms vanish in Eq. (13), which contracts to the simpler case of $(1 + K)\frac{d^2H}{d\eta^2} - \left(\left(\frac{3m-1}{m+1}\right)H\frac{dF}{d\eta} - F\frac{dH}{d\eta}\right) = 0$, as studied analytically by Willson⁶¹.

Fig. 4 depicts the temperature (θ) response to viscous heating parameter, i.e., Eckert number, $Ec = u^2/c\Delta T$. Viscous heating is a significant effect in polymer coating flows. When a highly viscous liquid (e.g., polycarbonate suspension) is deformed in a flow field, some of the work of deformation is converted into heat by internal friction, as observed by Winter⁶². The Prandtl number assumed is high ($Pr = 100$). The momentum diffusivity is therefore much lower than thermal diffusivity in the flow and the thermal conductivity is also very low. In other words, heat is convected much slower than momentum. This results in amplifying the contribution of the primary and secondary shear rates, as simulated

in the term, $(1 + K)Ec\left\{\left\langle\frac{d^2F^2}{d\eta^2}\right\rangle + \left\langle\frac{dG^2}{d\eta}\right\rangle\right\}$, in the

thermal boundary layer Eq. (14). When $Ec = 0$, viscous dissipation effects are negated, and temperatures are minimized. The implication is that omission of viscous heating leads to an under-prediction in temperature field. Increasing values of Eckert number (which relates the kinetic energy dissipated in the flow to the boundary layer enthalpy difference) leads to a rise in thermal boundary layer thickness. A further point of note is that, in the present analysis, both primary and secondary contributions to viscous dissipation are included, whereas in the vast majority of studies in the literature, only primary velocity contribution is incorporated in models.

Fig. 5 visualizes the evolution in temperature with Φ (heat sink), for the case of $m = 0.3$ (general wedge flow). This wedge case corresponds to a wedge angle of approximately 83 degrees, i.e., a steep wedge configuration). In all profiles, the maximum temperature is computed at the wedge surface (wall) and for $\Phi > -1$, monotonic decays into the free stream are observed. For the case $\Phi = -2$, a

kink appears in the near-wall region, and thereafter a weak ascent ensues to the free stream. Stronger heat sink implies greater removal of heat from the boundary layer via the wall. This technique, as noted earlier, is used in polymer fabrication processes to circumvent the supplementary heat build-up associated with viscous dissipation. A more homogeneous thermal diffusion is therefore produced in manufactured products, and thermal boundary layer thickness is significantly decreased with greater heat sink effect. The absence of a heat sink (Φ) would clearly result in higher temperatures, which are undesirable in materials processing operations^{16,17}. A heat source ($\Phi > 0$) is also unsuitable for thermal control in such flows, and is therefore not considered here.

Fig. 6 illustrates the impact of pressure gradient parameter (wedge angle parameter, m) on primary velocity distribution, $dF/d\eta$. As noted earlier, with $m = 0$, Case II is retrieved, i.e., flow past a semi-infinite horizontal surface (flat plate) also known as Blasius flow). For $m = 1.0$, Case III is obtained, i.e., forward stagnation point flow (wedge angle is 180 degrees) adjacent to a vertical surface. The intermediate cases, i.e., $m = 0.3$ (wedge), 0.7 (wedge), correspond to wedge angles of 83 degrees and 148 degrees, respectively. The latter case therefore implies extremely steep wedge geometry. Increasing wedge parameter clearly significantly reduces temperatures and cools the regime. Thermal boundary layer thickness is also depleted. The classical monotonic ascent for Blasius flow ($m = 0$) is increasingly warped with greater wedge parameter. However, for $m = 0.3$, positive values of primary velocity are still sustained. Negative velocities, i.e., flow reversal in the boundary layer is only induced, in close proximity to the wedge surface for $m = 0.7$, and further amplified for the vertical plate case. Again, asymptotically smooth profiles are computed in the free stream confirming the specification of a sufficiently large infinity boundary condition in the free stream (edge of the boundary layer).

Fig. 7 illustrates the variation in secondary velocity, G , with wedge parameter, m . It is evident that an oscillatory topology is present for the Blasius flow case ($m = 0$), which is progressively damped with increasing wedge parameter values. Increasing m also serves to strongly suppress secondary velocity values, i.e., decelerate the secondary flow. However, very strong reverse flow is induced for the wider wedge angle case ($m = 0.7$), and further exacerbated for the stagnation flow case ($m = 1.0$). Maximum secondary velocity is computed for the Blasius case at intermediate distance from the wedge surface. Minimum secondary velocity is generated very close to the wedge surface for the stagnation flow case. The wedge parameter m fea-

tures in the secondary momentum, Eq. (12) via the coupled term, $-\frac{2m}{m+1}G\frac{dF}{d\eta}$. As such, secondary

velocity distribution is clearly very sensitive to modification in wedge parameter, i.e., the geometry of the flow. Instability is clearly maximized for the vertical plate scenario (stagnation case).

Fig. 8 shows the impact of wedge parameter, m , on angular velocity, H . It is evident that a much more controlled response is computed compared with the secondary velocity. Peak values of micro-rotation, H , arise in oscillatory topology present in the Blasius flow case ($m = 0$), which is progressively damped with increasing wedge parameter values. Positive micro-rotation arises at the wedge surface ($\eta = 0$) only for the wide (obtuse) wedge case

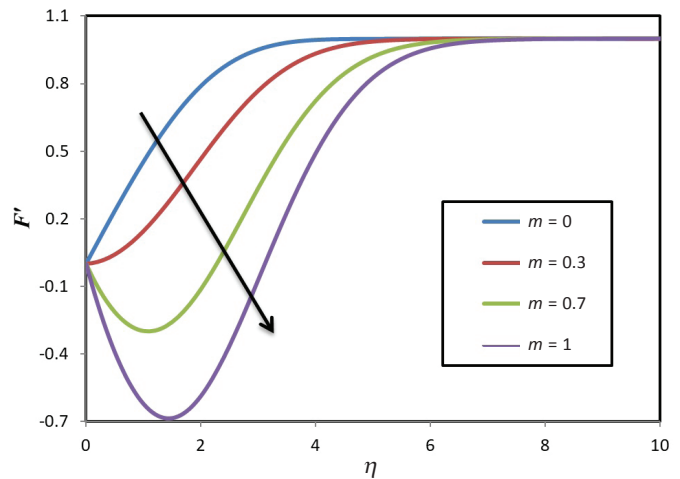


Fig. 6 – $dF/d\eta$ (primary velocity) versus η for $K = 0.5$, $I = 0.5$, $\Phi = -0.5$ (heat sink), $Pr = 100$ (weak polymers), $Ec = 0.2$, with $m = 0$ (Blasius flow), 0.3 (wedge), 0.7 (wedge), 1.0 (stagnation flow)

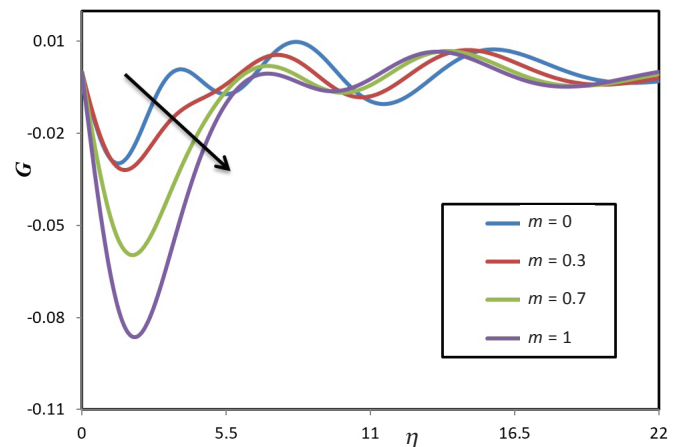


Fig. 7 – G (secondary velocity) versus η for $K = 0.5$, $I = 0.5$, $\Phi = -0.5$ (heat sink), $Pr = 100$ (weak polymers), $Ec = 0.2$, with $m = 0$ (Blasius flow), 0.3 (wedge), 0.7 (wedge), 1.0 (stagnation flow)

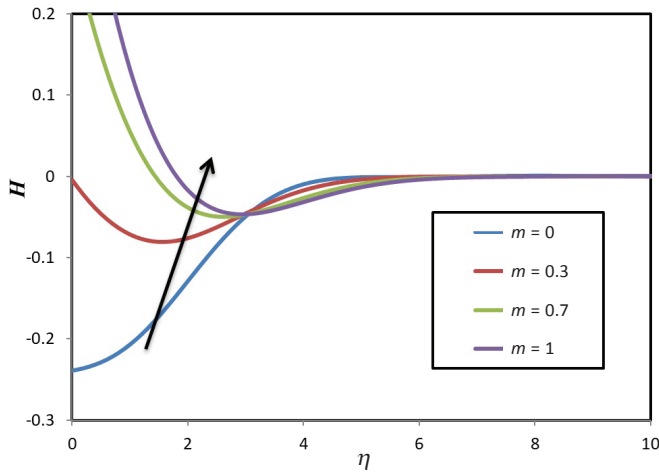


Fig. 8 – H (angular velocity) versus η for $K = 0.5$, $I = 0.5$, $\Phi = -0.5$ (heat sink), $Pr = 100$ (weak polymers), $Ec = 0.2$, with $m = 0$ (Blasius flow), 0.3 (wedge), 0.7 (wedge), 1.0 (stagnation flow)

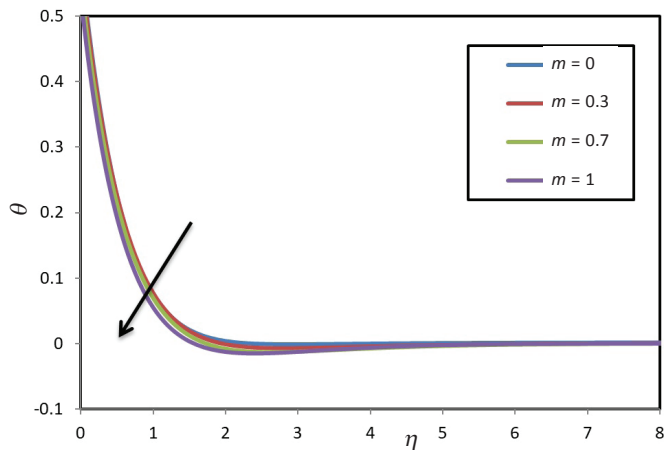


Fig. 9 – θ (temperature) versus η for $K = 0.5$, $I = 0.5$, $\Phi = -0.5$ (heat sink), $Pr = 100$ (weak polymers), $Ec = 0.2$, with $m = 0$ (Blasius flow), 0.3 (wedge), 0.7 (wedge), 1.0 (stagnation flow)

($m = 0.7$), and the forward stagnation case ($m = 1$). For the acute wedge case, ($m = 0.3$), and Blasius case, ($m = 0$), weakly negative and strongly negative microrotation (i.e., reverse spin of the microelements), respectively, are observed at the wedge surface (wall). For $m < 1$, smooth decays are computed from the wall to the free stream. However, for $m = 1$, a distinct monotonic growth arises. In all cases, asymptotically smooth profiles converge at $\eta \sim 6$. In the near-wall zone, significant reduction in microrotation is witnessed. However, further from the wall into the boundary layer, there is a slight upsurge in microrotation for the Blasius case. The wedge parameter (also known as the Falkner-Skan power-law parameter) features extensively in several terms in the angular momentum boundary layer, Eq. (13),

$$-\left(\left(\frac{3m-1}{1}\right)H \frac{dF}{d\eta} - F \frac{dH}{d\eta}\right) \text{ and } -\frac{2KI}{m+1} \left(2H + \frac{d^2F}{d\eta^2}\right)$$

The wedge parameter therefore exerts a marked influence on rotary motions of the micro-elements. Generally, the increase in wedge parameter, however, produces significant deceleration in angular velocity and reduces angular momentum boundary layer thickness. This trend has also been observed by Ishak *et al.*⁶³ although with no physical interpretation and with a greater focus on multiple solutions of purely mathematical interest.

Fig. 9 shows the influence of wedge parameter, m , on temperature, θ , again for the dissipative polymer flow case ($Ec = 0.2$, $Pr = 100$). Increasing m clearly decreases temperatures weakly, with the greatest modification at some distance from the wedge surface. Thermal boundary layer thickness is therefore marginally reduced with larger wedge parameters. A slightly cooler regime is produced for the forward stagnation flow case ($m = 1$) compared with the Blasius flat plate case ($m = 0$), with wedge cases falling in between these extremes. Although m does arise in the energy (thermal) boundary layer,

$$\text{Eq. (14) via the terms } (m-1) \frac{dF}{d\eta}, (m-1)F \frac{d\theta}{d\eta},$$

since m is a function of Hartree pressure gradient parameter (β^*), the dominant impact is on linear (primary, secondary) velocity fields and angular velocity, rather than the temperature field. With regard to polymer coating systems, enhanced temperature control (improved cooling) is clearly achieved via the forward stagnation scenario rather than any other geometrical case, although, as noted earlier, (Fig. 5), heat sink (Φ) has a much more profound impact and induces much stronger cooling.

Figs. 10–12 illustrate the influence of Eringen micropolar, i.e., vortex viscosity parameter (K) on primary velocity, secondary velocity, angular velocity, and temperature, respectively, again for the dissipative polymer acute wedge case. A strong deceleration in primary flow, (Fig. 10), is induced which is contrary to the conventional response in flat plate boundary layer flows, as noted by Hayat *et al.*³¹, Gupta *et al.*³² and Nath⁶⁰, among others. The customary drag-reduction effect of micropolar fluids in flat plate flows is therefore not achieved for wedge flows, since the primary velocity, $dF/d\eta$, is reduced. However, at any value of Eringen parameter, backflow is not induced and consistently smooth ascents from the wedge surface to the free stream are computed for primary velocity. The Newtonian fluid case ($K = 0$) achieves maximum acceleration, and the strongly micropolar case, ($K = 2$), the greatest deceleration. Evidently, the modified shear term,

$$\text{i.e., } (1+K) \frac{d^3F}{d\eta^3} \text{ and coupling term, } +K \frac{dH}{d\eta},$$

which feature the Eringen micropolar parameter,

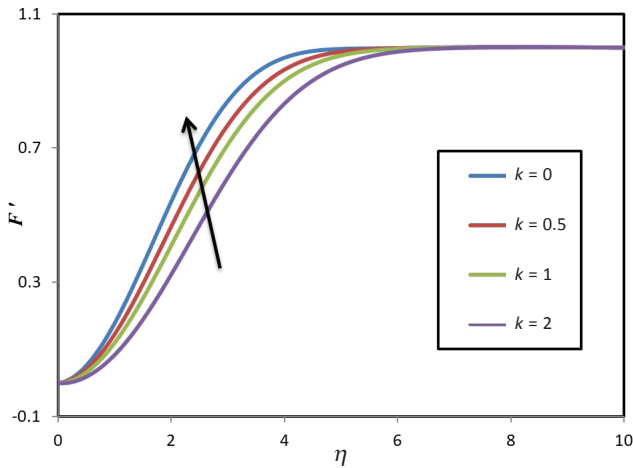


Fig. 10 – $-dF/d\eta$ (primary velocity) versus η for $I = 0.5$, $\Phi = -0.5$ (heat sink), $Pr = 100$ (weak polymers), $m = 0.3$ (general wedge flow), $Ec = 0.2$, with $K = 0$ (Newtonian), 0.5, 1, 2, 5

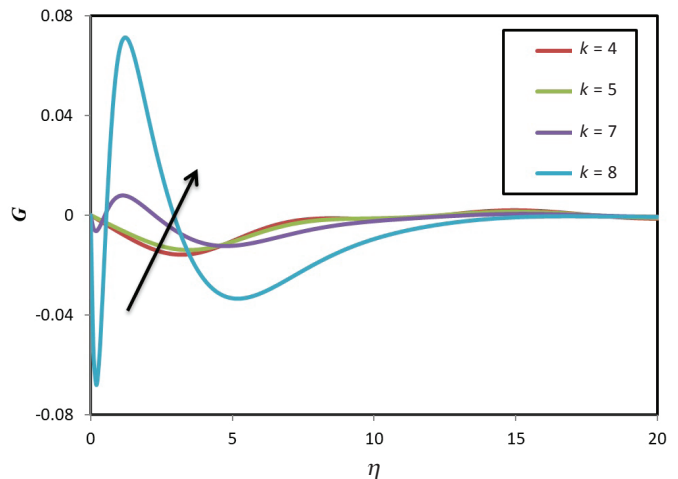


Fig. 11 – G (secondary velocity) versus η for $I = 0.5$, $\Phi = -0.5$ (heat sink), $Pr = 100$ (weak polymers), $m = 0.3$ (general wedge flow), $Ec = 0.2$, with $K = 4, 5, 7, 8$

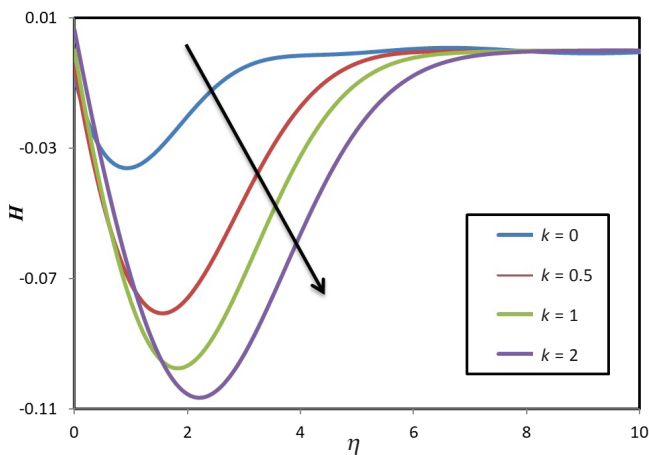


Fig. 12 – H (angular velocity) versus η for $I = 0.5$, $\Phi = -0.5$ (heat sink), $Pr = 100$ (weak polymers), $m = 0.3$ (general wedge flow), $Ec = 0.2$, with $K = 0$ (Newtonian), 0.5, 1, 2, 5

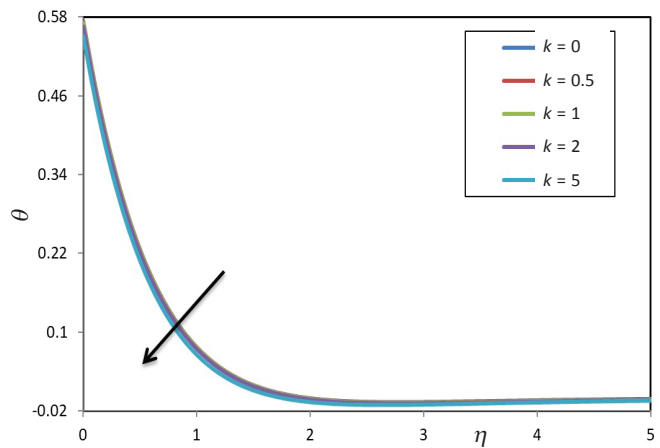


Fig. 13 – θ (temperature) versus η for $I = 0.5$, $\Phi = -0.5$ (heat sink), $Pr = 100$ (weak polymers), $m = 0.3$ (general wedge flow), $Ec = 0.2$, with $K = 0$ (Newtonian), 0.5, 1, 2, 5

produce considerable modifications in the primary velocity field. Primary momentum boundary layer thickness is therefore increased with micropolar vortex viscosity, i.e., higher values of K . Conversely, a strong enhancement in secondary velocity, G , is computed at higher values of Eringen micropolar parameter, K , as observed in Fig. 11. This behaviour is most evident near the wedge surface. The micropolarity effect is imparted to the secondary flow

field via the term, $(1+K)\frac{d^2G}{d\eta^2}$, in Eq. (12). The

reverse effect is generated away from the wall with a progressive suppression in secondary velocity. This switch in response is not sustained in the primary flow for which a consistent deceleration in primary flow is observed throughout the boundary layer (Fig. 10). Fig. 12 shows that a weak increase in angular velocity is produced near the wall with increasing Eringen micropolar parameter. However

quickly this pattern is altered and a short distance into the boundary layer transverse to the wedge surface, substantial reversal in angular velocity is induced with increasing vortex viscosity (higher K values), and this is maintained into the freestream. Generally, angular momentum boundary layer thickness is therefore elevated for strongly micropolar fluids. Finally, in Fig. 13, a distinct and consistent reduction in temperature is produced with increasing K values. Increasing vortex viscosity relative to the Newtonian dynamic viscosity (K defines the ratio of these two viscosities) results in a cooling of the regime and diminishing in thermal boundary layer thickness. This cooling effect has also been computed for flat plate micropolar convection flows^{31,32} and is achieved also for the wedge flow case ($m = 0.3$).

Tables 2–5, as noted earlier, provide the influence of wedge parameter (m), Eringen vortex

viscosity parameter (K), and micro-inertia density parameter (I) on $\frac{d^2F(0)}{d\eta^2}$, i.e., $(\text{Re})^{1/2}C_{f_{sp}}$ (primary shear stress), $\frac{dG(0)}{d\eta}$, i.e., $(\text{Re})^{1/2}C_{f_{ss}}$ (secondary shear stress), $\frac{dH(0)}{d\eta}$, i.e., $(\text{Re})^{1/2}M_w$ (wall couple stress) and $\frac{d\theta(0)}{d\eta}$, i.e., $(\text{Re})^{-1/2}Nu$ (Nusselt number function), respectively. Table 2 shows that with increasing m , K , I , primary skin friction is consistently decreased, i.e., flow deceleration is induced. This concurs with the primary velocity graph described earlier, and shows that drag-reduction is not achieved with wedge configurations ($m = 0.1, 0.3$), whereas it is attained with flat plate Blasius flow ($m = 0$). Table 3 demonstrates that secondary skin friction is also decreased (flow retardation) with increasing wedge parameter (m), whereas it is increased with Eringen vortex viscosity parameter (K), and also very weakly increased with micro-inertia density parameter (I). Table 4 reveals that dimensionless wall couple stress, i.e., angular velocity gradient at the wedge surface (wall), is significantly reduced with increasing wedge parameter (m), Eringen vortex viscosity parameter (K), and micro-inertia density parameter (I). Maximum wall couple stress is therefore associated always with the Blasius flow scenario, ($m = 0$). Finally, a significant enhancement in Nusselt number is observed in Table 5, with elevation in wedge parameter (m), whereas no tangible modification is produced with increase in Eringen vortex viscosity parameter (K) or micro-inertia density parameter (I). Heat transfer to the wall is therefore assisted with greater pressure gradient effect, implying a cooling in the boundary layer. Microstructural non-Newtonian effects are found to have no marked influence on convection of heat to the wall, i.e., they do not noticeably alter the relative contribution of convection to conduction heat transfer at the wedge surface.

Conclusion

Motivated by applications in thermal polymer coating processes, a mathematical model for axisymmetric micropolar convection boundary layer flow from a two-dimensional wedge with heat sink and viscous dissipation effects has been presented. Blasius flow and forward stagnation flow have also been considered as special cases of the general wedge (Falkner-Skan) flow. The non-dimensionalized ordinary differential boundary value problem has been solved with the semi-analytical/numerical

homotopy analysis method (HAM). A full and rigorous validation of HAM solutions has also been conducted with the Nakamura tridiagonal method (NTM). A 10th order of HAM approximation has been employed which achieves rapidly convergent and highly accurate solutions. Primary and secondary velocity, angular velocity, and temperature response to a variation in micropolar rheological (vortex viscosity) parameter, Eckert number (viscous dissipation), Falkner-Skan pressure gradient (i.e., wedge power law) parameter, and heat sink parameter at a high Prandtl number of 100, representative of polymers, have been computed and visualized graphically. Primary and secondary skin friction, micropolar wall couple stress, and Nusselt number distributions have also been tabulated for selected parameters. The influence of these parameters on momentum and thermal boundary layer thicknesses has also been addressed. The present study has shown that:

(i) Primary skin friction and wall couple stress are both reduced with increasing wedge parameter (m), Eringen vortex viscosity parameter (K), and micro-inertia density parameter (I).

(ii) Secondary skin friction is decreased with increasing wedge parameter (m), whereas it is elevated with Eringen vortex viscosity parameter (K), and also slightly enhanced with greater micro-inertia density parameter (I).

(iii) Nusselt number is enhanced substantially with greater wedge parameter (m), whereas it is not modified with either Eringen vortex viscosity parameter (K) or micro-inertia density parameter (I).

(iv) Temperature and thermal boundary layer thickness are both suppressed with increasing wedge parameter (they are maximized for the Blasius flow case of vanishing wedge parameter).

(v) Temperature and thermal boundary layer thickness is strongly depleted with increasing wall heat sink effect, i.e., the regime is cooled, which is beneficial to temperature regulation in polymer coating dynamics.

(vi) Strong reverse spin is generated in the microrotation with increasing vortex viscosity (higher K values), and angular momentum boundary layer thickness is increased.

(vii) Temperature is reduced (as is thermal boundary layer thickness) with increasing K values, confirming the cooling characteristics of micropolar fluids, which may be exploited in thermal regulation of polymer coating systems.

HAM has been shown to be a very versatile and accurate analytical tool for simulating nonlinear multiphysical micropolar coating flow problems. The current study has however been confined to isothermal flow, and has also neglected slip effects

which may arise in polymeric hydrophobic near-wall phenomena. Future investigations will examine time-dependent micropolar flows⁶⁴ and multiple wall slip (hydrodynamic and thermal slip), and mass diffusion effects⁶⁵, and will be reported imminently.

Nomenclature

$A_{i=1...4}$	– Nakamura matrix coefficients, –
$B_{i=1...4}$	– Nakamura matrix coefficients, –
$C_{i=1...4}$	– Nakamura matrix coefficients, –
c	– Positive constant, –
c_i	– Arbitrary constants, –
c_p	– Specific heat at constant pressure (isobaric), $\text{J kg}^{-1} \text{K}^{-1}$
$C_{fx,p}$	– Dimensionless primary skin friction, –
$C_{fx,s}$	– Dimensionless secondary skin friction, –
Ec	– Eckert number, –
f	– Body force per unit mass vector, N kg^{-1}
$F(\eta)$	– Dimensionless stream function, –
$F_0(\eta)$	– Initial guess of $F(\eta)$, –
$F_m^*(\eta)$	– Solution of m^{th} order deformation equation for $F(\eta, \zeta)$, –
\dot{G}	– Angular velocity (microrotation or gyration) vector, radians s^{-1}
$G(\eta)$	– Dimensionless secondary velocity, –
$G_0(\eta)$	– Initial guess of $G(\eta, \zeta)$, –
$G_m^*(\eta)$	– Solution of m^{th} order deformation equation for $G(\eta, \zeta)$, –
$H(\eta)$	– Dimensionless angular velocity (microrotation), –
$H_0(\eta)$	– Initial guess of $H(\eta, \zeta)$, –
$H_m^*(\eta)$	– Solution of m^{th} order deformation equation for $H(\eta, \zeta)$, –
\hbar	– Control parameter for F , G , H and θ , –
I	– Micro-inertia density dimensionless parameter, –
j	– Micro-inertia density, m^{-1}
k	– Thermal conductivity of the micropolar fluid, $\text{W m}^{-1} \text{K}^{-1}$
K	– Vortex viscosity parameter, $\text{kg m}^{-1} \text{s}^{-1}$
l	– Body couple per unit mass vector, N m kg^{-1}
L	– Arbitrary scale length, m
Li	– Auxiliary linear operator, –
$m = \beta^*/(2 - \beta^*)$	– Hartree pressure gradient parameter, –
m_w	– Dimensional wall couple stress, –
N	– Angular velocity (microrotation) component in the x - y plane, radians s^{-1}
N_u	– Local Nusselt number, –
N_i	– Auxiliary non-linear operator, –
P	– Thermodynamic pressure, Pa
p	– Embedding parameter, –

Pr	– Prandtl number, –
Q	– Heat sink parameter, –
q_w^*	– Rate of heat transfer, W m^{-2}
Re	– Reynolds number, –
$S_{i=1...4}$	– Nakamura source terms, –
T	– Fluid temperature, K
T_∞	– Ambient fluid (free stream), K
u	– Translational velocity along the x -direction, m s^{-1}
$U = cx^m$	– External velocity, m s^{-1}
v	– Translational velocity along the y -direction, m s^{-1}
\dot{V}	– Translational velocity vector, m s^{-1}
x, y, z	– Cartesian coordinates, m

Greek symbols

α, β	– Spin gradient viscosity coefficients for micropolar fluids, $\text{kg m}^{-1} \text{s}^{-1}$
$\gamma = (\mu + \kappa/2)j$	– Eringen spin gradient viscosity, $\text{kg m}^{-1} \text{s}^{-1}$
μ	– Dynamic viscosity, $\text{m}^2 \text{s}^{-1}$
λ	– Eringen second order viscosity coefficient, $\text{kg m}^{-1} \text{s}^{-1}$
ρ	– Mass density of micropolar fluid, kg m^{-3}
κ	– Vortex viscosity coefficient, $\text{kg m}^{-1} \text{s}^{-1}$
$\theta(\eta)$	– Dimensionless temperature function, –
$\theta_0(\eta)$	– Initial guess of $\theta(\eta, \zeta)$, –
$\theta_m^*(\eta)$	– Solution of m^{th} order deformation equation for $\theta(\eta, \zeta)$, –
η	– Pseudosimilarity coordinate in the y -direction, –
τ_x	– Primary dimensional wall shear stress, N m^{-2}
τ_z	– Secondary dimensional wall shear stress, N m^{-2}
Φ	– Heat sink parameter (negative), –
$\Omega = \pi\beta^*$	– Total angle of the wedge, radians

Subscripts

w	– Wall conditions
∞	– Ambient condition

Superscripts

'	– Prime denotes the derivative with respect to η
---	---

ACKNOWLEDGEMENTS

The authors are thankful to both reviewers for their useful and constructive comments which have helped to improve the present article.

References

1. Falkner, V. M., Skan, S. W., Some approximate solutions of the boundary layer equation, *Philos. Mag.* **12** (1931) 865. doi: <https://doi.org/10.1080/14786443109461870>
2. Eddieson, J., Wedge and cone flows of viscoelastic liquids, *AIChE Journal* **19** (1973) 377. doi: <https://doi.org/10.1002/aic.690190229>
3. Jacob, N. A., Ishak, A., Pop, I., Falkner–Skan problem for a static or moving wedge in nanofluids, *Int. J. Therm. Sci.* **50** (2011) 133. doi: <https://doi.org/10.1016/j.ijthermalsci.2010.10.008>
4. Hsu, C.-C., Viscoelastic flow past a wedge with a soluble coating, *J. Fluid Mech.* **27** (1967) 445. doi: <https://doi.org/10.1017/S0022112067000473>
5. Billingham, J., King, A. C., Surface-tension-driven flow outside a slender wedge with an application to the inviscid coalescence of drops, *J. Fluid Mech.* **533** (2005) 193. doi: <https://doi.org/10.1017/S0022112005004349>
6. Su, X., Zheng, L., Zhang, X., Zhang, J., MHD mixed convective heat transfer over a permeable stretching wedge with thermal radiation and Ohmic heating, *Chem. Eng. Sci.* **78** (2012) 1. doi: <https://doi.org/10.1016/j.ces.2012.04.026>
7. Abbasbandy, S., Naz, R., Hayat, T., Alsaedi, A., Numerical and analytical solutions for Falkner–Skan flow of MHD Maxwell fluid, *Appl. Math. Comput.* **242** (2014) 569. doi: <https://doi.org/10.1016/j.amc.2014.04.102>
8. Martin, M. J., Boyd, I. D., Falkner–Skan flow over a wedge with slip boundary conditions, *AIAA J. Thermophys. Heat Trans.* **24** (2010) 263. doi: <https://doi.org/10.2514/1.43316>
9. Bég, O. A., Bég, T. A., Takhar, H. S., Raptis, A., Mathematical and numerical modeling of non-Newtonian thermo-hydrodynamic flow in non-Darcy porous media, *Int. J. Fluid Mech. Research* **31** (2004) 1. doi: <https://doi.org/10.1615/InterJFluidMechRes.v31.i1.10>
10. Hossain, M. A., Bhowmick, S., Gorla, R. S. R., Unsteady mixed-convection boundary layer flow along a symmetric wedge with variable surface temperature, *Int. J. Eng. Sci.* **44** (2006) 607. doi: <https://doi.org/10.1016/j.ijengsci.2006.04.007>
11. Kim, Y. J., The Falkner–Skan wedge flows of power-law fluids embedded in a porous medium, *Transp. Porous Media* **44** (2001) 267. doi: <https://doi.org/10.1023/A:1010769604457>
12. Rashidi, M. M., Bég, O. A., Rastegari, M. T., A study of non-Newtonian flow and heat transfer over a non-isothermal wedge using the Homotopy Analysis Method, *Chem. Eng. Commun.* **199** (2012) 231. doi: <https://doi.org/10.1080/00986445.2011.586756>
13. Gorla, R. S. R., Unsteady heat transfer in laminar non-Newtonian boundary layer over a wedge, *AIChE J.* **28** (1982) 56. doi: <https://doi.org/10.1002/aic.690280109>
14. Zueco, J., Bég, O. A., Network simulation solutions for laminar radiating dissipative magneto-gas dynamic heat transfer over a wedge in non-Darcian porous regime, *Math. Comput. Mod.* **50** (2009) 439. doi: <https://doi.org/10.1016/j.mcm.2009.05.028>
15. Singh, V., Bougher, T. L., Weathers, A., Cai, Y., Bi, K., Pettes, M. T., Altman, D. H., High thermal conductivity of chain-oriented amorphous polythiophene, *Nat. Nanotechnol.* **9**(5) (2014) 384. doi: <https://doi.org/10.1038/nnano.2014.44>
16. Shaukatullah, H., Gaynes, M. A., Comparative evaluation of various types of heat sinks for thermal enhancement of surface mount plastic packages, *Int. J. Micro. Electron. Packag.* **18** (1995) 252.
17. Cheng, W. T., Huang, C. N., Unsteady flow and heat transfer on an accelerating surface with blowing or suction in the absence and presence of a heat source or sink, *Chem. Eng. Science* **59** (2004) 771. doi: <https://doi.org/10.1016/j.ces.2003.11.019>
18. Kumar, H., Heat transfer in MHD boundary-layer flow through a porous medium, due to a non-isothermal stretching sheet, with suction, radiation, and heat annihilation, *Chem. Eng. Comm.* **200** (2013) 895. doi: <https://doi.org/10.1080/00986445.2012.727509>
19. Hassan, H., Regnier, N., Pujos, C., Defaye, G., The effect of viscous dissipation on the polymer temperature during injection molding 5th European Thermal-Sciences Conference, Delft, The Netherlands, June (2008). doi: <https://doi.org/10.1002/pen.21077>
20. Aydin, O., Effect of viscous dissipation on the heat transfer in forced pipe flow. Part 1: Hydro dynamically and thermally fully developed flow, *Energ. Convers. Manage.* **46** (2005) 757. doi: <https://doi.org/10.1016/j.enconman.2004.05.004>
21. Ahmad R., Khan, W. A., Effect of viscous dissipation and internal heat generation/absorption on heat transfer flow over a moving wedge with convective boundary condition, *Heat Transf-Asian Res.* **42** (2013) 589. doi: <https://doi.org/10.1002/htj.21055>
22. Munir, A., Shazad, A., Khan, M., Convective flow of Sisko fluid over a wedge with viscous dissipation, *J. Braz. Soc. Mech. Sci. Eng.* **38**(2) (2015) 581. doi: <https://doi.org/10.1007/s40430-015-0310-z>
23. Bég, O. A., Zueco, J., Takhar, H. S., Unsteady magnetohydrodynamic Hartmann–Couette flow and heat transfer in a Darcian channel with Hall current, ion-slip, viscous and Joule heating effects: Network numerical solutions, *Comm. Nonlinear Sci. Numer. Simulat.* **14** (2009) 1082. doi: <https://doi.org/10.1016/j.cnsns.2008.03.015>
24. Chhabra, R. P., Richardson, J. F., *Non-Newtonian flow and applied rheology: Engineering applications*. Oxford: Butterworth-Heinemann, (2011). doi: <https://doi.org/10.1016/B978-0-7506-0-X0001-7>
25. Riaz, A., Ellahi, R., Bhatti, M. M., Marin, M., Study of heat and mass transfer in the Eyring–Powell model of fluid propagating peristaltically through a rectangular compliant channel, *Heat Transf. Res.* **50**(16) (2019) 1539. doi: <https://doi.org/10.1615/HeatTransRes.2019025622>
26. Ray, A. K., Vasu, B., Hydrodynamics of non-Newtonian Spriggs fluid flow past an impulsively moving plate. In *Applications of Fluid Dynamics*, Springer, Singapore (2018) 95-107. doi: https://doi.org/10.1007/978-981-10-5329-0_7
27. Majeed, A., Zeeshan, A., Bhatti, M. M., Ellahi, R., Heat transfer in magnetite (Fe₃O₄) nanofluid suspended with conventional fluids refrigerant-134a (C₂H₂F₄), kerosene (C₁₀H₂₂) and water (H₂O) under the impact of dipole, *Heat Transf. Res.* **51** (2020) 217. doi: <https://doi.org/10.1615/HeatTransRes.2019029919>
28. Eringen, A. C., Theory of micropolar fluids, *J. Math. Mech.* **6** (1966) 1. doi: <https://doi.org/10.1512/iumj.1967.16.16001>
29. Eringen, A. C., *Micro-continuum Field Theories- II: Fluent Media*, Springer, Berlin (2001).

30. Bég, O. A., Bhargava, R., Rashidi, M. M., Numerical Simulation in Micropolar Fluid Dynamics, Lambert Academic, Saarbrücken, Germany, (2011).
31. Bég, O. A., Prasad, V. R., Vasu, B., Reddy, N. R., Li, Q., Bhargava, R., Free convection heat and mass transfer from an isothermal sphere to a micropolar regime with sores/dufour effects, *Int. J. Heat Mass Transf.* **54** (2011) 9. doi: <https://doi.org/10.1016/j.ijheatmasstransfer.2010.10.005>
32. Gupta, D., Kumar, L., Bég, O. A., Singh, B., Finite element analysis of transient heat and mass transfer in microstructural boundary layer flow from porous stretching sheet, *Comp. Thermal Sci.* **6** (2) (2014) 155. doi: <https://doi.org/10.1615/ComputThermal-Scien.2014008401>
33. Prasad, V. R., Gaffar, S. A., Bég, O. A., Heat and mass transfer of a nanofluid from a horizontal cylinder to a micropolar fluid, *AIAA J. Thermophysics. Heat Transfer* **29** (2015) 127. doi: <https://doi.org/10.2514/1.T4396>
34. Pažanin, I., Suarez-Grau, F. J., Analysis of the thin film flow in a rough domain filled with micropolar fluid, *Comput. Math. Appl.* **68** (12) (2014) 1915. doi: <https://doi.org/10.1016/j.camwa.2014.10.003>
35. Bég, O. A., Zueco, J., Chang, T. B., Numerical analysis of hydromagnetic gravity-driven thin film micropolar flow along an inclined plane, *Chem. Eng. Commun.* **198** (2010) 312. doi: <https://doi.org/10.1080/00986445.2010.512534>
36. Liao, S., A new branch of solutions of boundary-layer flows over an impermeable stretched plate, *Int. J. Heat Mass Transf.* **49** (2005) 2529. doi: <https://doi.org/10.1016/j.ijheatmasstransfer.2005.01.005>
37. Bég, O. A., Zueco, J., Norouzi, M., Davoodi, M., Joneidi, A. A., Elsayed, A. F., Network and Nakamura tridiagonal computational simulation of electrically-conducting biopolymer micro-morphic transport phenomena, *Comput. Biol. Med.* **44** (2014) 44. doi: <https://doi.org/10.1016/j.compbiomed.2013.10.026>
38. Vasu, B., Gorla, R. S. R., Bég, O. A., Murthy, P. V. S. N., Prasad, V. R., Kadir, A., Unsteady flow of a nanofluid over a sphere with non-linear Boussinesq approximation, *AIAA J. Thermophys. and Heat Transf. (USA)* (2018) 1. doi: <https://doi.org/10.2514/1.T5516>
39. Vasu, B., Ray, A. K., Bég, O. A., Gorla, R. S. R., Magneto-bioconvection flow of a Casson thin film with nanoparticles over an unsteady stretching sheet: HAM and GDQ computation, *Int. J. Numer. Method H.* **29** (2019) 4277. doi: <https://doi.org/10.1108/HFF-02-2019-0158>
40. Tripathi, D., Bég, O. A., Peristaltic transport of Maxwell viscoelastic fluids with a slip condition: Homotopy analysis of gastric transport, *J. Mech. Med. Biol.* **15** (2015) 1550021.42. doi: <https://doi.org/10.1142/S0219519415500219>
41. Gao, L., Wang, J., Zhong, Z., Analytical solutions of surface acoustic wave propagation in functionally graded plates with the homotopy analysis method, *IEEE Int. Ultrasonics Symp.*, Orlando, Florida, USA 18-21 October (2011) 1696. doi: <https://doi.org/10.1109/ULTSYM.2011.0423>
42. Vasu, B., Gorla, R. S. R., Murthy, P. V. S. N., Bég, O. A., Entropy analysis on convective film flow of power-law fluid with nanoparticles along an inclined plate, *J. Appl. Mech. Tech. Phys.* **60** (2019) 1. doi: <https://doi.org/10.1134/S0021894419050067>
43. Ray, A. K., Vasu, B., Bég, O. A., Gorla, R. S. R., Murthy, P. V. S. N., Homotopy semi-numerical modelling of non-Newtonian nanofluid transport external to multiple geometries using a revised Buongiorno model, *Invent.* **4** (2019) 54. doi: <https://doi.org/10.3390/inventions4040054>
44. Liao, S., Homotopy analysis method in nonlinear differential equations, Beijing: Higher education press, (2012). doi: <https://doi.org/10.1007/978-3-642-25132-0>
45. Liao, S., Chwang, A. T., Application of homotopy analysis method in nonlinear oscillations. *ASME J. Appl. Mech.* **65** (1998) 914. doi: <https://doi.org/10.1115/1.2791935>
46. Srinivas, J., Bég, O. A., Homotopy study of entropy generation in magnetized micropolar flow in a vertical parallel plate channel with buoyancy effect, *Heat Transf. Res.* **49**(6) (2018) 529. doi: <https://doi.org/10.1615/HeatTransRes.2018018305>
47. Arafat, A. A. M., Rida, S. Z., Mohamed, H., An application of the homotopy analysis method to the transient behavior of a biochemical reaction model, *Inf. Sci. Lett.* **3**(1) (2014) 29. doi: <https://doi.org/10.12785/isl/030104>
48. Ray, A. K., Vasu, B., Murthy, P. V. S. N., Gorla, R. S., Non-similar solution of Eyring–Powell fluid flow and heat transfer with convective boundary condition: Homotopy analysis method, *International Journal of Appl. Computat. Math.* **6**(1) (2020) 16. doi: <https://doi.org/10.1007/s40819-019-0765-1>
49. Shukla, N., Rana, P., Bég, O. A., Singh, B., Kadir, A., Homotopy study of magnetohydrodynamic mixed convection nanofluid multiple slip flow and heat transfer from a vertical cylinder with entropy generation, *Propuls. Power Res.* **8**(2) (2019) 147. doi: <https://doi.org/10.1016/j.jprr.2019.01.005>
50. Ray, A. K., Vasu, B., Gorla, R. S. R., Homotopy simulation of non-Newtonian Spriggs fluid flow over a flat plate with oscillating motion, *Int. J. Appl. Mech. Eng.* **24**(2) (2019) 359. doi: <https://doi.org/10.2478/ijame-2019-0023>
51. Vasu, B., Ray, A. K., Numerical study of Carreau nanofluid flow past vertical plate with the Cattaneo-Christov heat flux model, *Int. J. Numer. Method H.* **29** (2019) 702. doi: <https://doi.org/10.1108/HFF-03-2018-0104>
52. Chaht, F. L., Kaci, A., Houari, M. S. A., Tounsi, A., Bég, O. A., Mahmoud, S. R., Bending and buckling analyses of functionally graded material (FGM) size-dependent nanoscale beams including the thickness stretching effect, *Steel and Compos. Struct.* **18**(2) (2015) 425. doi: <https://doi.org/10.12989/scs.2015.18.2.425>
53. Bég, O. A., Prasad, V. R., Vasu, B., Numerical study of mixed bioconvection in porous media saturated with nanofluid and containing oxytactic micro-organisms, *J. Mech. Med. Biol.* **13** (2013) 1350067. doi: <https://doi.org/10.1142/S021951941350067X>
54. Jashim Uddin, M., Bég, O. A., Ismail, A. I. M., Group analysis and numerical computation of magneto-convective non-Newtonian nanofluid slip flow from a permeable stretching sheet, *Appl. Nanosci.* **4** (2014) 897. doi: <https://doi.org/10.1007/s13204-013-0274-1>
55. Bég, O. A., Numerical methods for multi-physical magnetohydrodynamics, Chapter 1, *New Developments in Hydrodynamics Research*, Nova Science, New York, September (2012) 1.
56. Nakamura, S., Iterative finite difference schemes for similar and non-similar boundary layer equations, *Adv. Eng. Softw.* **21** (1994) 123. doi: [https://doi.org/10.1016/0965-9978\(94\)90038-8](https://doi.org/10.1016/0965-9978(94)90038-8)

57. *Incropera, F. P., DeWitt, J. P., Bergman, T. L.*, Fundamentals of Heat and Mass Transfer, 6th EDN., Wiley, USA (2006).
58. *Hassanien, I. A., Salama, A. A.*, Flow and heat transfer of a micropolar fluid in an axisymmetric stagnation flow on a cylinder, *Energ. Convers. and Manage.* **38** (1997) 301.
doi: [https://doi.org/10.1016/S0196-8904\(96\)00032-5](https://doi.org/10.1016/S0196-8904(96)00032-5)
59. *Mahmoud, M. A., Waheed, S. E.*, MHD flow and heat transfer of a micropolar fluid over a stretching surface with heat generation (absorption) and slip velocity, *J. Egypt. Math. Soc.* **20** (2012) 20.
doi: <https://doi.org/10.1016/j.joems.2011.12.009>
60. *Nath, G.*, Similar solutions for the incompressible laminar boundary layer with pressure gradient in micropolar fluids, *Rheol. Acta* **14** (1975) 850.
doi: <https://doi.org/10.1007/BF01521414>
61. *Willson, A. J.*, Boundary layers in micropolar liquids, *Proc. Camb. Phil. Soc.* **67** (1970) 469.
doi: <https://doi.org/10.1017/S0305004100045746>
62. *Winter, H. H.*, Viscous dissipation in shear flows of molten polymers, *Adv. Heat Transf.* **13** (1977) 3.
doi: [https://doi.org/10.1016/S0065-2717\(08\)70224-7](https://doi.org/10.1016/S0065-2717(08)70224-7)
63. *Ishak, A., Nazar, R., Pop, I.*, Moving wedge and flat plate in a micropolar fluid, *Int. J. Eng. Sci.* **44** (2006) 1225.
doi: <https://doi.org/10.1016/j.ijengsci.2006.08.005>
64. *Bég, O. A., Ferdows, M., Karim, M. E., Hasan, M. M., Bég, T. A., Shamsuddin, M. D., Kadir, A.*, Computation of non-isothermal thermo-convective micropolar fluid dynamics in a Hall MHD generator system with non-linear distending wall, *Int. J. Appl. Comput. Math.* **6** (2020) 1.
doi: <https://doi.org/10.1007/s40819-020-0792-y>
65. *Bég, O. A., Bhargava, R., Sharma, S., Bég, T. A., Shamsuddin, M., Kadir, A.*, Numerical solutions for axisymmetric non-Newtonian stagnation enrobing flow, heat and mass transfer with application to cylindrical pipe coating dynamics, *Comput. Therm. Sci.* **12**(1) (2020) 79.
doi: <https://doi.org/10.1615/ComputThermalScien.2020026228>
66. *Ishak, Anuar, Roslinda Nazar, Ioan Pop*, MHD boundary-layer flow of a micropolar fluid past a wedge with constant wall heat flux, *Comm. Nonlinear Sci. Numer. Simulat.* **14**(1) (2009) 109.
doi: <https://doi.org/10.1016/j.cnsns.2007.07.011>